Boreal summer intraseasonal oscillation in a superparameterized GCM: effects of air-sea coupling and ocean mean state

Yingxia Gao[1,2], Nicholas P. Klingaman[2], Charlotte A. DeMott[3], Pang-Chi Hsu[1]

[1]Key Laboratory of Meteorological Disaster of Ministry of Education/Collaborative Innovation Center on Forecast and Evaluation of Meteorological Disasters/NUIST-UoR International Research Institute, Nanjing University of Information Science & Technology, Nanjing, China
[2]National Centre for Atmospheric Science-Climate and Department of Meteorology, University of Reading, Reading, United Kingdom
[3]Department of Atmospheric Science, Colorado State University, Fort Collins, Colorado, USA

Correspondence to: Pang-Chi Hsu (pangchi@nuist.edu.cn)

Abstract. The effect of air-sea coupling on the simulated boreal summer intraseasonal oscillation (BSISO) is examined using atmosphere—ocean-mixed-layer coupled (SPCAM3-KPP) and uncoupled configurations of the Super-Parameterized (SP) Community Atmospheric Model, version 3 (SPCAM3). The coupled configuration is constrained to either the observed ocean mean state or the mean state from the SP coupled configuration with a dynamic ocean (SPCCSM3), to understand the effect of mean state biases on the BSISO in the latter. All configurations overestimate summer mean subtropical rainfall and its intraseasonal variance. All configurations simulate realistic BSISO northward propagation over the Indian Ocean and western Pacific, in common with other SP configurations.

Constraining SPCAM3-KPP to the SPCCSM3 mean state reduces the overestimated BSISO variability, but also weakens BSISO propagation. Using the SPCCSM3 mean state also introduces a one-month delay to the BSISO seasonal cycle compared to SPCAM3-KPP with the observed ocean mean state, which matches well with the reanalysis. The phase relationship between intraseasonal rainfall and sea surface temperature (SST) is captured by all coupled models, but with a shorter delay between suppressed convection and warm SST relative to the reanalysis. Prescribing the 31-day smoothed SSTs from the SPCAM3-KPP simulations in SPCAM3 worsens the overestimated BSISO variance. This suggests that air-sea coupling improves the amplitude of the simulated BSISO. Based on a Taylor diagram, SPCCSM3 mean state SST biases and air-sea coupling both lead to higher simulated BSISO fidelity, largely due to their ability to suppress the overestimated subtropical BSISO variance.

1 Introduction

The intraseasonal oscillation (ISO) is the most vigorous sub-seasonal signal in the tropics (Zhang, 2005). It interacts closely with tropical climate and weather systems, such as the El Niño–Southern Oscillation (ENSO) and tropical cyclones (Kessler et al., 1995; Zhang and Gottschalck, 2002; Mcphaden, 2004; Wu et al., 2007), and even mid-latitude systems (Ding and Wang, 2007; Moon et al., 2013). Compared to the boreal winter ISO (i.e., the Madden and Julian Oscillation; MJO; Madden

and Julian, 1971, 1972), the boreal summer ISO (BSISO) shifts away from the equator to the Asian summer monsoon (ASM) region (Wang et al., 2006; Lau and Waliser, 2012). Thus, the BSISO is connected strongly to the onset, active and break phases of ASM (Yasunari, 1979; Annamalai and Slingo, 2001; Lau and Waliser, 2012). The frequency of extreme events

35   over the ASM region is also highly related to BSISO activity (Ren et al., 2013; Li et al., 2015; Hsu et al., 2016, 2017).

Realistic representations of the BSISO in climate models remain a challenge, although some improvements have been achieved in recent decades. Current state-of-art general circulation models (GCMs) still have difficulty to simulate properly the BSISO spatial pattern (Sperber and Annamalai, 2008; Sperber et al., 2013; Hu et al., 2017) and its northwest-southeast tilted rain band structure (Lin et al., 2006; Sabeerali et al., 2013). In contrast, the northward propagation, which is the most

40   significant feature of BSISO, is captured by more models. Fidelity for northward propagation improved in models that contributed to the Coupled Model Intercomparison Project (CMIP) phase 5, relative to the CMIP phase 3 (Sabeerali et al., 2013; Sperber et al., 2013). Most models with reasonable northward propagation also simulated a good eastward propagation along the equatorial Indian Ocean.

The representation of convection is largely responsible for the ability of GCMs to simulate BSISO characteristics

45   (Maloney and Hartmann, 2001; Randall et al., 2007; Jiang et al., 2016). Using the Hadley Centre atmospheric GCM (AGCM), Klingaman and Woolnough (2014) found that increasing the convective entrainment and detrainment rates considerably improved deficient MJO-like variability in the Indian and Pacific Oceans. In recent years, studies have shown that "superparameterized" GCMs have high fidelity for simulating ISO variability (Benedict and Randall, 2009; Jiang et al., 2015; Neena et al., 2017). In superparameterized GCMs, the traditional cumulus parameterization is replaced by a two-

50   dimensional cloud-resolving model in each grid column to calculate the cloud and radiation physics tendencies (Khairoutdinov and Randall, 2003; Khairoutdinov et al., 2005). By comparing different versions of the National Center for Atmospheric Research (NCAR) Community Atmospheric Model (CAM), DeMott et al. (2014) showed that the superparameterized CAM (SPCAM3) demonstrated better BSISO characteristics than CAM with the standard convective parameterization.

55   Besides the convective parameterization scheme, the effect of air–sea interaction on simulated ISO variability has also received growing attention. Many model studies report a substantially improved BSISO representations in coupled GCMs (CGCMs) compared to the corresponding AGCMs (Fu and Wang, 2004; Rajendran and Kitoh, 2006; Klingaman et al., 2008; DeMott et al., 2014). In contrast, Ajayamohan et al. (2011) found no changes in the BSISO properties with coupling. Peatman and Klingaman (2018) investigated the effect of air-sea coupling on the simulated Indian summer monsoon in the

60   UK Met Office Unified Model Global Ocean Mixed layer configuration (MetUM-GOML2.0), a similar model framework that used in this study. Coupling degraded the atmospheric basic state, but slightly improved the BSISO northward propagation.

Incorporating air-sea interaction in CGCMs inevitably introduces atmospheric and oceanic mean state biases. When studies compare CGCMs to AGCMs prescribed with observed SSTs (Kemball-Cook et al., 2002; Zhang et al., 2006; DeMott

65   et al., 2011; Roxy et al., 2013), the differences between simulations may largely come from mean-state differences, rather

than air-sea coupling. Due to the strong control on low-level moisture and convergence anomalies, mean state biases may degrade simulated intraseasonal variability (Hendon, 2000; Inness et al., 2003; Sperber et al., 2005; Bollasina and Ming, 2013). Using the National Centers for Environmental Prediction (NCEP) coupled Climate Forecast System (CFS) model, Seo et al. (2007) showed that BSISO development and propagation were largely improved when the CGCM cold SST bias

70   was removed via flux corrections. They suggested that the role of air-sea interactions would be more accurate under an ocean mean state with smaller SST biases. To reduce the mean-state differences between CGCMs and AGCMs, time-varying SST from CGCMs should be used to drive AGCMs (Fu and Wang, 2004; Seo et al., 2007; Levine and Turner, 2012; DeMott et al., 2015). However, this quantifies the role of air-sea coupling only under the biased CGCM mean state.

  Through flux correction techniques, CGCMs can be constrained to a given climatological ocean state. Such techniques are

75   more effective in CGCMs with simple ocean models, which lack ocean dynamics, as dynamics may interfere with the prescribed flux correction. Simple ocean models also lack coupled modes of variability, such as ENSO, feedbacks from which can influence the perceived effects of coupling on sub-seasonal variability (Klingaman and DeMott, 2020). CGCMs with simplified oceans are a useful tool to investigate the roles of air-sea coupling and mean-state biases in the simulation of BSISO. In this paper, we examine the role of air-sea interactions and mean state biases in the simulated BSISO using a

80   configuration of SPCAM3 coupled to a mixed-layer ocean model, constrained to observed ocean mean state and mean state from the superparameterized Community Climate System Model (CCSM), version 3 (SPCCSM3; Stan et al. 2010). The model experiments, validation data, and analysis methods are described in section 2. Section 3 analyses the influence of air-sea coupling and mean state biases in the spatial pattern and propagation of simulated BSISO. Results are discussed and summarized in sections 4 and 5, respectively.

85   2 Model, experiments and methods

2.1 Models

SPCAM3 (Khairoutdinov et al., 2005) is employed in this study, due to its high fidelity for the simulated ISO (Jiang et al., 2015; Neena et al., 2017). It has a horizontal resolution of T42 and a vertical resolution of 30 levels. The embedded 2-D cloud-process resolving model, used to calculate convective and radiative temperature and moisture tendencies, has 32

90   columns with a fine resolution (4km) (Khairoutdinov and Randall, 2003). To understand the role of air-sea interaction in the BSISO simulation, SPCAM3 is coupled to the Multi-Column K Profile Parameterization (MC-KPP) mixed-layer ocean model (referred to as "SPCAM3-KPP"). MC-KPP uses the KPP vertical mixing scheme of Large et al. (1994). It consists of many independent 1-D columns, with one column under each AGCM grid point to which it is coupled. Therefore, the horizontal resolution of MC-KPP is the same as SPCAM3. MC-KPP has a fine vertical resolution, with 100 points in a

95   1000m water column, 70 of which are in the top 300m, and a ~1m resolution in the upper 20m. Further details on SPCAM3-KPP can be found in Klingaman and DeMott (2020).

Since ocean dynamics are absent in MC-KPP, SPCAM3-KPP must be constrained to a reference ocean climatology, which can be taken from an observation-based dataset, an ocean model or a CGCM simulation. This makes MC-KPP an attractive option for investigating the role of air-sea coupling under different ocean mean states. To represent mean ocean dynamics and correct for biases in atmospheric surface fluxes, prescribed vertical profiles of heat and salt corrections are applied at each grid point and each timestep. These are computed from a 10-year SPCAM3-KPP "relaxation" simulation with a 15-day relaxation timescale towards the reference seasonal cycle of oceanic temperature and salinity. The daily climatology of corrections is then computed and imposed on a "free-running" coupled integration with no relaxation, which displays only small SST biases against the reference climatology (Fig. 1). Further details on the correction method can be found in Hirons et al. (2015), Peatman and Klingaman (2018) and Klingaman and DeMott (2020).

2.2 Experiments and validation data

Two pairs of atmospheric-only (SPCAM3) and coupled (SPCAM3-KPP) models are analysed to examine the role of air-sea coupling and mean state biases in the simulated BSISO (Table 1). These simulations are also analysed for the MJO in Klingaman and DeMott (2020). For brevity, we write SPCAM3 and SPCAM3-KPP as "SPA" and "SPK", respectively. All simulations are 50-year integrations. Next, we explain the setup of each experiment in detail.

To study the effect of mean state biases on the simulated BSISO, SPK is constrained to two ocean mean states: 1) the 1980–2009 climatology from the Smith and Murphy (2007) 3D ocean analysis; and 2) the climatology from a 20-year simulation of SPCCSM3 ("SPC" for short; Stan et al., 2010; DeMott et al., 2011, 2014). The former is considered as the observed ocean state (Fig. 1c), against which SPC shows large cold SST biases throughout the Indo-Pacific in boreal summer (Fig. 1f). These two coupled simulations are referred to as "SPK-OBS" and "SPK-SPC", respectively. To investigate the effect of air-sea interaction on the simulated BSISO under the observed ocean mean state, SPCAM3 is forced by the 31-day smoothed SST from SPK-OBS (hereafter "SPA-KOBS"). Similarly, we prescribe the 31-day smoothed SST from SPK-SPC to SPCAM3 to understand the air-sea coupling effect under the SPC mean state ("SPA-KSPC"). Table 1 summarises all four experiments.

All validation data in this study are from the European Centre for Medium-range Weather Forecasts (ECMWF) Interim (ERAI) reanalysis dataset (Dee et al., 2011). The daily variables used include: precipitation, outgoing longwave radiation (OLR), 850-hPa wind, surface variables related to latent heat and sensible heat (LH and SH) fluxes, and 3-D variables associated with moist static energy (MSE; Maloney, 2009). All the variables have the horizontal resolution of 1.5° ×1.5°; we analyse the period of 1986–2016 for compatibility with Gao et al. (2019).

2.3 Methods

The BSISO convective intensity is represented by 20–100-day-filtered variability of boreal summer (May–October) precipitation, OLR or MSE, depending on the process-oriented diagnostic applied. To reveal the overall propagation features of BSISO convection, lead-lag regression analysis is performed on area-averaged filtered precipitation. Since the Indian and

Pacific basins exhibit different basic states (Lau and Waliser, 2012), we compute propagation over one region in each basin:
130   the eastern Indian Ocean (80°E–90°E, 0°–10°N) and western Pacific (130°E–140°E, 0°–10°N).

DeMott et al. (2016) and Gao et al. (2019) provide a useful diagnostic method to quantitatively assess the contribution of intraseasonal SST variability to the MSE budget of ISO in boreal winter and boreal summer, respectively. We employ the same approach to understand oceanic feedbacks to the simulated BSISO, and compare these feedbacks to those in reanalysis data. Intraseasonal SST can affect atmospheric convection through modifying surface turbulent fluxes (LH and SH) and
135   hence MSE, via the near-surface gradients in specific humidity and temperature. Based on decomposition of surface bulk formulae (Weare et al., 1981), SST modulation of surface fluxes is represented as the difference between fluxes calculated using the full and 61-day smoothed SST. These SST-modulated fluxes are then projected onto column-integrated MSE and its tendency ($\langle m \rangle$ and $\partial \langle m \rangle / \partial t$) to reveal the oceanic feedback to the maintenance and propagation of BSISO convection, respectively. Further details can be found in DeMott et al. (2016) and Gao et al. (2019).

140   We employ the BSISO indices of Lee et al. (2013) to investigate the simulated convective features in each BSISO phase. Firstly, daily anomalies are computed as the departure from the climatological annual cycle (annual mean and first three harmonics) and a 120-day running mean. Multi-variate Empirical Orthogonal Function (MV-EOF) is then performed on the combination of OLR and u850 anomalies, each normalized by their respective area-mean standard deviation over the ASM region (40°E–160°E, 10°S–40°N) during boreal summer. The first two leading principal components (PC1 and PC2) define
145   the BSISO indices, which separate the BSISO life cycle into eight phases. For model results, normalized OLR and u850 anomalies are projected onto the observed EOF modes to obtain the model PCs. Model simulated BSISO phase composites are constructed based on these PCs (Sperber et al. 2013). Consistent with Lee et al. (2013), only strong BSISO events ($\sqrt{PC1^2 + PC2^2} > 1.5$) are selected for phase composites.

3 Results

150   ### 3.1 Mean state and intraseasonal variability

Previous studies indicate that ISO variability is closely related to the climatological state of convection (Wheeler and Kiladis, 1999; Sperber et al., 2000; Waliser et al., 2003). Thus, we firstly examine the summer mean precipitation and 850-hPa wind (Fig. 2). In ERAI, substantial rainfall appears over the ASM region where the average exceeds 8 mm/day (Fig. 2a). SPK-OBS overestimates subtropical rainfall (10°N–20°N), particularly in the western North Pacific (Figs. 2b and e), but
155   underestimates rainfall over the southern Indian Ocean, Maritime Continent and India north to 20°N. These precipitation biases are associated with low-level wind biases. Simulated mean westerlies extend into the western North Pacific, increasing convergence across the band of subtropical enhanced precipitation. In SPK-SPC (Fig. 2c), which is constrained to the cold climatological SPCCSM3 SST (Fig. 1d), rainfall reduces compared to that in SPK-OBS: wet biases are reduced while dry biases become more severe (Figs. 2e and f).

160   Figure 3 illustrates the standard deviation of intraseasonal SST and precipitation variability. SST variability is underestimated over the Indian Ocean and equatorial Pacific in all simulations. Over the off-equatorial Pacific, there is more intraseasonal SST variability in SPK-OBS but less SST variability in SPK-SPC (Figs. 3b and c). Prescribing the 31-day smoothed SST from SPK-OBS (SPK-SPC) to SPA-KOBS (SPA-KSPC), strongly reduces intraseasonal SST, as expected (Figs. 3d and e). The right-column panels in Fig. 3 show the intraseasonal rainfall from each dataset (Figs. 3f–j). Compared

165   to ERAI (Fig. 3f), all simulations significantly overestimate subtropical intraseasonal precipitation variability (10°N–20°N), where mean rainfall is also overestimated (Fig. 2). This reinforces that model BSISO biases are largely associated with incorrect representations of mean rainfall (Sperber and Annamalai, 2008; Sabeerali et al., 2013; Hu et al., 2017). The overestimation of intraseasonal rainfall in SPK-SPC (Fig. 3h) is smaller than that in SPK-OBS (Fig. 3g), consistent with the lower mean rainfall in SPK-SPC. SPA-KOBS (Fig. 3i) and SPA-KSPC (Fig. 3j) show increases in intraseasonal rainfall

170   relative to SPK-OBS and SPK-SPC, respectively. This indicates that both cold SST biases and air-sea coupling exert negative feedbacks to BSISO convection, and improve the simulated BSISO amplitude.

3.2 Northward propagation of BSISO

Lag regression analysis is employed to understand the simulated BSISO propagation in each experiment. Over the Indian Ocean, 80°E–90°E averaged intraseasonal precipitation is regressed onto the (80°E–90°E, 0°–10°N) averaged intraseasonal

175   precipitation time series (Fig. 4). In ERAI, the convective anomaly originates south of the equator and propagates southward to 10°S and northward into the Bay of Bengal (Fig. 4a). All simulations capture the northward propagation, confirming the high fidelity of SPCAM3 for simulating BSISO northward propagation (DeMott et al., 2014; Neena et al., 2017). However, the simulations fail to capture the southward branch. And the simulated strongest convection shifts northward (10°N) relative to ERAI (5°N). A weaker propagating signal is observed under the SPC mean state than under the observed mean state for

180   both SPK and SPA, especially over the subtropical regions from Lag 0 to Lag 20 (marked with black box; Figs. 4b and d; Figs. 4c and e). This is consistent with weaker BSISO variability under the SPC mean state (Figs. 3g–j), suggesting that cold tropical mean SST biases are unfavourable for BSISO variability and northward propagation. In SPA, the amplitude of convective maxima increases relative to SPK, but with weaker propagation (Figs. 4b–e). Air-sea coupling plays a similar role in BSISO convection under both observed and cold mean states: it damps BSISO amplitude but supports northward

185   propagation over the eastern Indian Ocean.

   The BSISO northward propagation over the western Pacific is shown in Fig. 5. In ERAI, the convection also originates south of equator, but propagates only north, into the western North Pacific (Fig. 5a). These characteristics are properly simulated by all experiments (Figs. 5b–e). As in the Indian Ocean, due to the large overestimation of subtropical BSISO variability, the simulated strongest convection moves north compared to ERAI. It is notable that considerable suppressed off-

190   equatorial convection leads the strongest convection by ~1 week, which degrades model performance. Over the western Pacific, mean-state biases also reduce the northward propagating signal in SPK-SPC (SPA-KSPC) relative to in SPK-OBS

(SPA-KOBS). Air-sea interaction plays little role in the BSISO northward propagation over the western Pacific, as there is no substantial difference between SPK and SPA under either ocean mean state (Figs. 5b–c; Figs. 5d–e).

3.3 Quantitative contributions of SST fluctuations to BSISO

195 The temporal and spatial evolutions of BSISO and SST variability over the Indian Ocean and western Pacific are shown in Figs. 6 and 7, respectively. Over the Indian Ocean, in ERAI, warm SSTs always lead enhanced convection, with maxima north/northeast of the convective center (Figs. 6a, f and k). The SST-rainfall phase relationship is properly represented in SPK and misrepresented in SPA. However, in more detail, SPK shows a shorter delay between suppressed convection and warm SST relative to ERAI. This suggests the ocean responds more quickly to BSISO convection in SPK than in ERAI,

200 which might be caused by the lack of ocean dynamics in MC-KPP. Alternatively, the high coupling frequency (15 minutes) and fine oceanic vertical resolution (~1m) in SPK may make the mixed-layer depth too sensitive to atmospheric convection. SST anomalies in SPA are small due to the 31-day smoothing applied (Figs. 6d, e, i, j, n, and o). Compared to SPK-OBS, the convective region becomes smaller under the SPC mean state or without air-sea coupling (SPK-SPC, SPA-KOBS and SPA-KSPC). To some degree, it reflects the negative (positive) role of mean state biases (air-sea interaction) in supporting the

205 propagating BSISO signal, in agreement with Fig. 4.

Over the western Pacific, SPK simulates well the ERAI phase relationship between the convection and SST anomalies: a near-quadrature relationship over the equatorial regions (Figs. 7a–c), but nearly out-of-phase over the off-equatorial regions (Figs. 7f–h and k–m). However, SPK produces substantial suppressed convection north of the active convection over the western North Pacific, consistent with Fig. 5. As a result, simulated warm SST appears north of the convective center, while

210 the ERAI SST maximum is always located northwest of the convective center. Imposing the SPC mean state weakens convection. In SPA, the intraseasonal SST is very small by design.

As revealed by Gao et al. (2019), intraseasonal SST can affect the BSISO by modulating surface LH and SH fluxes. The temporal and spatial distributions of SST-modulated fluxes are highly coherent with those of SST anomalies themselves (Gao et al., 2019; their Figs. 14 and 15). Therefore, the evolutions of SST anomalies shown in Figs. 6 and 7 can also roughly

215 reveal the evolutions of SST-modulated surface fluxes. By regressing the SST-modulated flux anomalies onto the BSISO MSE and the time rate of change of MSE ($\langle m \rangle$ and $\partial \langle m \rangle / \partial t$), Figure 8 illustrates the "SST effect" on the maintenance and propagation of convection, respectively. In ERAI, intraseasonal SST supports $\langle m \rangle$ in the central Indian Ocean and Bay of Bengal but destroys $\langle m \rangle$ in the western North Pacific (Fig. 8a). The inter-basin differences are linked to the differences in SST-convection phase relationships (Gao et al. 2019). However, in SPK, simulated SST anomalies largely damp the

220 convection over both the Bay of Bengal and western North Pacific (Figs. 8b and c), because of the quicker response of the SPK ocean to BSISO convection, combined with the erroneously strong suppressed convection just before the active phase. In SPK, the negative SST effect on $\langle m \rangle$ agrees with the stronger BSISO variability in SPA (Fig. 3i; Fig. 3j) than in SPK (Fig. 3g; Fig. 3h) over the subtropics. SST anomalies have similar effects on BSISO propagation under the observed and SPC mean states, with some amplitude difference. The simulated SST anomalies in SPK favor convection propagation (Figs. 8g

and h), but with a smaller contribution (8–12%) than in ERAI (12–20%). This is caused by the incorrect phase relationship between the simulated BSISO and SST anomalies (Figs 6 and 7). A weak SST effect on the BSISO can still be found in SPA (Figs. 8d, e, i, and j), as these simulations retain some intraseasonal SST variability (Fig. 3). In summary, SST variability enhances the simulated amplitude of BSISO variability by suppressing the excessive subtropical convection and contributes to the propagation of convection over the entire BSISO region.

3.4 BSISO indices

Propagating BSISO characteristics can also be examined using the BSISO indices. Figure 9 shows the annual cycle of variance of each of the first four PCs from ERAI and model simulations. Since EOF analysis is only applied to May–October, PC time series for November–April are obtained by projecting OLR and u850 anomalies onto the same EOF patterns.

In ERAI, PCs have a similar seasonal cycle as those from Lee et al. (2013). PC1 has the largest variance throughout boreal summer (Fig. 9a). It increases sharply from late April, maximising in August, followed by PC2 with about half a month delay. In contrast to PC1 and PC2, PC3 exhibits most of its variance in early summer (May–June). PC4 also has a broad peak, but its amplitude is much smaller than the other PCs. SPK-OBS produces a similar seasonal cycle of PC1 as ERAI, except for deficient variance in August–September, which largely reduces the amplitude difference between the first two PCs (Fig. 9b). Simulated PC1 also increases abruptly from late April, with a half-month delay between PC1 and PC2, which matches ERAI well. However, PC1 in SPK-SPC begins to increase in late May (Fig. 9c), about one month later than ERAI and SPK-OBS. The variance of the first two PCs in SPK-SPC has a much narrower peak and tails off from early July, without a second peak in October. This suggests that cold SST error leads to a late onset of BSISO activity, and also strongly degrades the annual cycle of BSISO activity. In both SPK simulations, the amplitude of PC3 is smaller than that of PC4, which indicates that the order of those simulated PCs is reversed. All model simulations show a similarly poor ability to simulate PC3 and PC4. Therefore, hereafter we only focus on PC1 and PC2. Removing air-sea coupling in SPA increases significantly the strength of PC1 relative to SPK. This suggests that the role of air-sea coupling in suppressing BSISO variability is mainly expressed through damping variability in PC1.

Based on the PC1 and PC2 time series, the BSISO life cycle is separated into eight phases, which represents the canonical northward propagating BSISO (Annamalai and Sperber, 2005; Wang et al., 2005). Figure 10 shows the phase composite of anomalous precipitation and 850-hPa wind from ERAI and SPK-OBS. SPK-OBS displays a similar evolution of the structure of convection and circulation as in ERAI, but with significant amplitude differences. The simulated circulation also matches well with the simulated convection: easterlies (westerlies) occur to the north (south) of the ascent; cyclonic (anticyclonic) circulations coincide with the active (suppressed) off-equatorial convection. However, the northwest-southeast tilted rainfall band in SPK-OBS is more zonal than in ERAI (Fig. 10e and m), largely due to the poor representation of BSISO variability over the western Pacific. In ERAI, most strong BSISO events occur in phases 2, 5 and 7. In contrast, in SPK-OBS, a stronger preference for simulated strong BSISO events appear in off-equatorial regions (phases 3, 4, 7, and 8)

rather than in near-equatorial regions (phases 1, 2, 5, and 6). It implies that the BSISO variability is largely determined by the propagating BSISO signal (Sperber et al., 2013; Neena et al., 2017).

We further compute the frequency of strong BSISO events in each phase from each dataset (Fig. 11). Overall, there are
260 fewer strong BSISO events in the simulations (25–30%) than in ERAI (~33%), although the amplitude of simulated precipitation associated with these events is much larger. Consistent with Fig. 10, in ERAI, phases 2, 5 and 7 show the highest frequencies, while in SPK-OBS, most strong simulated BSISO events occur in phases 3, 4, 7, and 8. Comparing SPK-SPC and SPK-OBS shows that the SPC ocean mean state has little consistent effect on the frequency of BSISO events. Removing air-sea coupling in SPA further increases the frequency of strong BSISO events in off-equatorial regions (phases
265 3, 4, 7, and 8), associated with the greater intraseasonal convective variability in SPA relative to SPK.

To more quantitatively evaluate the performance of each simulation, we construct Taylor diagrams over the Indian Ocean (50°E–100°E, 10°S–20°N) and western Pacific (110°E–160°E, 0°–30°N), respectively (Fig. 12). These diagrams provide pattern correlation coefficients and root-mean-square-errors of the simulated intraseasonal precipitation against ERAI intraseasonal precipitation in each BSISO phase. Over the Indian Ocean, the fidelity of each simulation varies from phase to
270 phase (Fig. 12a). Generally, higher pattern correlations appear in equatorial phases (phases 1, 2, 5 and 6) than in off-equatorial phases (phases 3, 4, 7 and 8). The area-averaged rainfall variability is overestimated in almost all phases, with largest amplitude biases in phases 3 and 6 (1.5–2.25 of the standard deviation of ERAI). Overall, SPK-SPC outperforms SPK-OBS, largely due to its smaller amplitude biases compared to ERAI. Under the observed ocean mean state, air-sea coupling improves the simulation fidelity in phases 1, 3, 7, and 8. Under the SPC ocean mean state, coupling greatly
275 improves the simulated BSISO life cycle over the Indian Ocean, except for phase 2.

In almost all simulations, higher pattern correlations are found over the western Pacific (0.7–0.9) than over the Indian Ocean (0.5–0.9), but with much larger overestimations of amplitude (Fig. 12b). The overall simulation performance is ranked as follows: SPK-SPC, SPA-KSPC, SPK-OBS and SPA-KOBS. Simulations with the SPC ocean mean state perform better than those under the observed ocean mean state, in terms of both amplitude and distribution. Since the excessive
280 subtropical rainfall variability is the biggest error in SPCAM3, the underlying cold SSTs largely weaken convection, which helps to reduce the amplitude biases and improve the pattern correlation with ERAI. Air-sea coupling improves model performance under both mean states, particularly in suppressing the overestimated simulated BSISO variability over the western North Pacific.

4 Discussion

285 Despite the large correct SST-rainfall phase relationship in SPK simulations, a shorter delay between suppressed convection and warm SST exists relative to the reanalysis. This may be associated with the configuration of the MC-KPP ocean (lack of ocean dynamics, high coupling frequency and fine vertical resolution). As a consequence, it is easy to surmise the effect of air-sea coupling on the amplitude of convection, while its effect on the propagation is not obvious. Overall, in SPK,

intraseasonal SST anomalies largely damp intraseasonal subtropical convection variability and make a smaller contribution
290 (8–12%) to $\partial\langle m\rangle/\partial t$ than in ERAI (12–20%). Propagation is slightly enhanced in SPK relative to SPA over the Indian Ocean, however, coupling makes nearly no difference to the propagating signal over the western Pacific. This may be related to the larger underestimation of the contribution of intraseasonal SST to $\partial\langle m\rangle/\partial t$ over the western Pacific than over the Bay of Bengal (Fig. 8). More importantly, it implies that atmospheric internal processes are essential to the propagation of convection, since SPCAM3 simulates BSISO propagation well even without coupling or sub-seasonal SST variability (Gao
295 et al. 2019).

Stan et al. (2010) and Neena et al. (2017) reported that SPCCSM3 showed better ISO simulation skill than SPCAM3 with prescribed observed SST. In our experiments, the BSISO variability is similar in SPK-OBS and SPA-KOBS and in SPK-SPC and SPA-KSPC, which suggests a limited role for air-sea coupling in the simulated BSISO. Comparing SPK-OBS and SPK-SPC strongly suggests that the ocean mean-state biases in SPC improve BSISO amplitude and spatial distribution. This
300 implies that mean-state bias in SPC, not sub-seasonal air-sea coupled feedbacks, may be the primary reason for the improved BSISO in SPCCSM3 relative to SPCAM3. However, while the SPC mean state improves the amplitude and spatial pattern of simulated BSISO convection, it also weakens northward propagation. By examining Figs. 1g–h, these amplitude/spatial pattern and propagating differences between SPK-SPC and SPK-OBS may be related to the stronger horizontal SST gradients in SPK-SPC, since the pattern of mean state column water vapor biases closely follows that of mean SST biases
305 (DeMott et al., 2019). Stronger meridional SST gradients in SPC may largely suppress the overestimated subtropical rainfall than in SPK-OBS. SPC also seems to reduce the zonal SST (moisture) gradient that plays an essential role in $\partial\langle m\rangle/\partial t$ for both the boreal winter and boreal summer ISO, leading to less propagating BSISO signal (Jiang, 2017; Jiang et al., 2018; Gao et al., 2019). Thus, as suggested by Seo et al. (2007) and Klingaman and Woolnough (2014), it is important to control for the effect of mean-state biases as well as its gradients when evaluating the influence of air-sea coupling on the simulated
310 ISO (DeMott et al., 2019).

In CGCMs with dynamical oceans, it is also important to consider the effects of inter-annual SST variability (such as ENSO), due to its strong control on sub-seasonal variability, particularly on the boreal winter MJO (Weaver et al., 2011; Kapur and Zhang, 2012; Klingaman and DeMott, 2020). We note that none of the simulations considered here represent ENSO or other coupled modes of inter-annual variability, as the MC-KPP ocean model lacks the requisite ocean dynamics.
315 By using the same simulations, Klingaman and DeMott (2020) found that the intensity and propagation of the boreal-winter MJO was strongly suppressed in SPCAM3-KPP under the SPC ocean mean state, while here the SPC ocean mean state enhances BSISO amplitude and only slightly weakens propagation. Klingaman and DeMott (2020) found that the including of the SPC ENSO variability on top of the SPC mean state substantially strengthened the MJO, suggesting that the strong MJO in SPCCSM3 arose from an excessively intense response to ENSO. The effect of ENSO is not considered here, which
320 could be a subject for further study.

5 Summary

This study investigates the role of oceanic mean-state biases and air-sea coupling in simulating the BSISO by coupling the Superparameterized Community Atmospheric Model (SPCAM3) to the Multi-Column K Profile Parameterization (MC-KPP) mixed-layer ocean. To diagnose the sensitivity to the ocean mean state, SPCAM3-KPP is constrained to either the observed

325 ocean mean state or the ocean mean state from the coupled configuration of SPCAM3 with a dynamical ocean (SPCCSM3; "SPC" for short). The SPC mean state introduces substantial cold SST biases across the Indo-Pacific. To diagnose the sensitivity to air-sea coupling under each mean state, SPCAM3 is driven by the 31-day running mean SST from each SPCAM3-KPP simulation.

Systematic errors in SPCAM3 result in overestimated subtropical summer mean rainfall and intraseasonal variability. This

330 overestimation is greatly reduced with coupling, or with the SPC ocean mean state. Lag regression composites show that the simulated convection exhibits realistic northward propagation over both the Indian Ocean and western Pacific. However, the strongest convective center shifts north relative to reanalysis. The SPC ocean mean state degrades the propagating BSISO signal in both coupled and uncoupled simulations, relative to simulations that use the observed ocean mean state. Air-sea coupling slightly enhances the strength of the propagating signal under both ocean mean states. The coupled simulations

335 capture a reasonable SST-rainfall phase relationship, but with warm SSTs shifting toward the suppressed convection relative to the reanalysis. Intraseasonal SST variability plays a similar role in the BSISO MSE budget in the coupled simulations, regardless of mean state: it damps subtropical convection and favors BSISO northward propagation, but with a smaller contribution (8–12%) than the reanalysis (12–20%).

The simulation skill of propagating BSISO characteristics is also examined by using BSISO indices. Experiments with the

340 observed ocean mean state produce a realistic annual cycle of BSISO variance, while a one-month delay to the onset of BSISO activity is found in simulations with the SPC mean state. Air-sea coupling weakens convective variability mainly through suppressing the first EOF mode. Different from the reanalysis, all model simulations favour strong BSISO activity in off-equatorial regions, associated with the intense subtropical variability. Simulations under the SPC ocean mean state produce an improved BSISO than those under the observed ocean mean state, in both the amplitude and pattern correlation

345 of anomalous precipitation. Air-sea coupling improves the BSISO fidelity in most phases. The enhancement of simulated BSISO by the ocean mean state and air-sea coupling largely arises from suppressing the erroneously strong subtropical convection.

In our study, air-sea coupling has a similar effect on the simulated BSISO under different oceanic background states, suggesting that the role of coupling may largely depend on the phase relationship between the convection and SST anomalies.

350 Compared to daily coupling frequency between the atmosphere and ocean components of CGCMs, improved fidelity for the BSISO simulation is shown in CGCMs with sub-daily coupling frequency (Woolnough et al., 2007; Klingaman et al., 2011; Hu et al., 2015). In our study, the ocean tends to respond quickly to the atmospheric convection, which may be associated with the sensitive mixed layer depth due to the absent ocean dynamics in KPP. Therefore, to better understand the role of

coupling in the simulated ISO, efforts should aim to simulate a realistic phase relationship between the ISO convection and
355 SST anomalies.

Code and data availability. All model outputs are available on the U.K. JASMIN collaborative research analysis facility
(http://www.jasmin.ac.uk). Access to data can be obtained by contacting Nicholas Klingaman (nicholas.klingaman@ncas.ac.uk). Data
used to reproduce the figures and associated code can be found at https://doi.org/10.6084/m9.figshare.c.4874406.v2
360

Competing interests: The authors have no competing interests to declare.

Author contributions. YG and PCH developed the code, conducted the analysis, and wrote the manuscript. NPK and CAD designed and
performed SPCAM3-KPP simulations presented in the paper. All authors gave comments and contributed to the development of the
365 manuscript.

Competing interests. The authors declare that they have no conflict of interest.

Acknowledgements. YG and PCH are supported by the National Key R&D Program of China (2018YFC1505804) and NUIST-UoR Open
370 Project. NPK is supported by an Independent Research Fellowship from the UK Natural Environment Research Council (NE/L010976/1)
and a grant from the NOAA Modeling, Analysis, Predictions and Projections program (NA16OAR4310071). CAD is supported by the
National Science Foundation (NSF 1445191) and the NOAA Modeling, Analysis, Predictions and Projections program
(NA16OAR4310094). ERAI reanalysis data are obtained from http://apps.ecmwf.int/datasets.

375 **References**

Ajayamohan, R. S., Annamalai, H., Luo, J.-J., Hafner, J. and Yamagata, T.: Poleward propagation of boreal summer
intraseasonal oscillations in a coupled model: Role of internal processes, Clim. Dyn., 37(5–6), 851–867,
https://doi.org/10.1007/s00382-010-0839-6, 2011.

Annamalai, H. and Slingo, J. M.: Active / break cycles: Diagnosis of the intraseasonal variability of the Asian summer
380 monsoon, Clim. Dyn., 18(1–2), 85–102, https://doi.org/10.1007/s003820100161, 2001.

Annamalai, H. and Sperber, K. R.: Regional heat sources and the active and break phases of boreal summer intraseasonal
(30–50 day) variability, J. Atmos. Sci., 62(8), 2726–2748, https://doi.org/10.1175/JAS3504.1, 2005.

Benedict, J. J. and Randall, D. A.: Structure of the Madden–Julian oscillation in the superparameterized CAM, J. Atmos. Sci.,
66(11), 3277–3296, https://doi.org/10.1175/2009JAS3030.1, 2009.

385 Bollasina, M. A. and Ming, Y.: The general circulation model precipitation bias over the southwestern equatorial Indian
Ocean and its implications for simulating the South Asian monsoon, Clim. Dyn., 40(3–4), 823–838,
https://doi.org/10.1007/s00382-012-1347-7, 2013.

Dee, D. P., Uppala, S. M., Simmons, A. J., Berrisford, P., Poli, P., Kobayashi, S., Andrae, U., Balmaseda, M. A., Balsamo, G., Bauer, P., Bechtold, P., Beljaars, A. C. M., van de Berg, L., Bidlot, J., Bormann, N., Delsol, C., Dragani, R., Fuentes, M.,
390   Geer, A. J., Haimberger, L., Healy, S. B., Hersbach, H., Hólm, E. V., Isaksen, L., Kållberg, P., Köhler, M., Matricardi, M., McNally, A. P., Monge-Sanz, B. M., Morcrette, J.-J., Park, B.-K., Peubey, C., de Rosnay, P., Tavolato, C., Thépaut, J.-N. and Vitart, F.: The ERA-Interim reanalysis: Configuration and performance of the data assimilation system, Q. J. Roy. Meteorol. Soc. 137(656), 553–597, https://doi.org/10.1002/qj.828, 2011.

DeMott, C. A., Stan, C., Randall, D. A., Kinter, J. L. and Khairoutdinov, M.: The Asian monsoon in the superparameterized
395   CCSM and Its relationship to tropical wave activity, J. Climate, 24(19), 5134–5156, https://doi.org/10.1175/2011JCLI4202.1, 2011.

DeMott, C. A., Stan, C., Randall, D. A. and Branson, M. D.: Intraseasonal variability in coupled GCMs: The roles of ocean feedbacks and model physics, J. Climate, 27(13), 4970–4995, https://doi.org/10.1175/JCLI-D-13-00760.1, 2014.

DeMott, C. A., Klingaman, N. P., Tseng, W.-L., Burt, M. A., Gao, Y., and Randall, D. A.: The convection connection: How
400   ocean feedbacks affect tropical mean moisture and MJO propagation, J. Geophys. Res. Atmos., 124(22), 11910–11931, https://doi.org/10.1029/2019JD31015, 2019.

DeMott, C. A., Klingaman, N. P. and Woolnough, S. J.: Atmosphere-ocean coupled processes in the Madden-Julian oscillation, Rev. Geophys., 53(4), 1099–1154, https://doi.org/10.1002/2014RG000478, 2015.

DeMott, C. A., Benedict, J. J., Klingaman, N. P., Woolnough, S. J. and Randall, D. A.: Diagnosing ocean feedbacks to the
405   MJO: SST-modulated surface fluxes and the moist static energy budget, J. Geophys. Res. Atmos., 121(14), 8350–8373, https://doi.org/10.1002/2016JD025098, 2016.

Ding, Q. and Wang, B.: Intraseasonal teleconnection between the summer Eurasian wave train and the Indian monsoon, J. Climate, 20(15), 3751–3767, https://doi.org/10.1175/JCLI4221.1, 2007.

Fu, X. and Wang, B.: Differences of boreal summer intraseasonal oscillations simulated in an atmosphere–ocean coupled
410   model and an atmosphere-only model, J. Climate, 17, 1263–1271, 2004.

Gao, Y., Klingaman, N. P., DeMott, C. A. and Hsu, P.: Diagnosing ocean feedbacks to the BSISO: SST-modulated surface fluxes and the moist static energy budget, J. Geophys. Res. Atmos., 124, 146–170, https://doi.org/10.1029/2018JD029303, 2019.

Hendon, H. H.: Impact of air–sea coupling on the Madden–Julian oscillation in a general circulation model, J. Atmos. Sci.,
415   57(24), 3939–3952, https://doi.org/10.1175/1520-0469(2001)058<3939:IOASCO>2.0.CO;2, 2000.

Hirons, L. C., Klingaman, N. P. and Woolnough, S. J.: MetUM-GOML1: a near-globally coupled atmosphere–ocean-mixed-layer model, Geosci. Model Dev., 8(2), 363–379, https://doi.org/10.5194/gmd-8-363-2015, 2015.

Hsu, P.-C., Lee, J.-Y. and Ha, K.-J.: Influence of boreal summer intraseasonal oscillation on rainfall extremes in southern China, Int. J. Climatol., 36(3), 1403–1412, https://doi.org/10.1002/joc.4433, 2016.

420   Hsu, P.-C., Lee, J.-Y., Ha, K.-J. and Tsou, C.-H.: Influences of boreal summer intraseasonal oscillation on heat waves in monsoon Asia, J. Climate, 30(18), 7191–7211, https://doi.org/10.1175/JCLI-D-16-0505.1, 2017.

Hu, W., Duan, A. and Wu, G.: Impact of subdaily air–sea interaction on simulating intraseasonal oscillations over the tropical Asian monsoon region, J. Climate, 28(3), 1057–1073, https://doi.org/10.1175/JCLI-D-14-00407.1, 2015.

Hu, W., Duan, A. and He, B.: Evaluation of intra-seasonal oscillation simulations in IPCC AR5 coupled GCMs associated with the Asian summer monsoon, Int. J. Climatol., 37, 476–496, https://doi.org/10.1002/joc.5016, 2017.

Inness, P. M., Slingo, J. M., Guilyardi, E. and Cole, J.: Simulation of the Madden–Julian oscillation in a coupled general circulation model. Part II: The role of the basic state, J. Climate, 16(3), 365–382, https://doi.org/10.1175/1520-0442(2003)016<0365:SOTMJO>2.0.CO;2, 2003.

Jiang, X.: Key processes for the eastward propagation of the Madden-Julian Oscillation based on multimodel simulations. J. Geophys. Res. Atmos., 122, 755–770, https://doi.org/10.1002/2016JD025955, 2017.

Jiang, X., Adames, A. F., Zhao, M., Waliser, D., and Maloney, E.: A unified moisture moist framework for seasonality of MJO propagation. J. Climate, 31, https://doi.org/10.1175/JCLI-D-17-0671.1, 2018.

Jiang, X., Waliser, D. E., Xavier, P. K., Petch, J., Klingaman, N. P., Woolnough, S. J., Guan, B., Bellon, G., Crueger, T., DeMott, C., Hannay, C., Lin, H., Hu, W., Kim, D., Lappen, C.-L., Lu, M.-M., Ma, H.-Y., Miyakawa, T., Ridout, J. A., Schubert, S. D., Scinocca, J., Seo, K.-H., Shindo, E., Song, X., Stan, C., Tseng, W.-L., Wang, W., Wu, T., Wu, X., Wyser, K., Zhang, G. J. and Zhu, H.: Vertical structure and physical processes of the Madden-Julian oscillation: Exploring key model physics in climate simulations, J. Geophys. Res. Atmos., 120(10), 4718–4748, https://doi.org/10.1002/2014JD022375, 2015.

Jiang, X., Zhao, M., Maloney, E. D. and Waliser, D. E.: Convective moisture adjustment time scale as a key factor in regulating model amplitude of the Madden-Julian oscillation, Geophys. Res. Lett., 43(19), 10,412-10,419, https://doi.org/10.1002/2016GL070898, 2016.

Kapur, A. and Zhang, C.: Multiplicative MJO forcing of ENSO, J. Climate, 25(23), 8132–8147, https://doi.org/10.1175/JCLI-D-11-00609.1, 2012.

Kemball-Cook, S., Wang, B. and Fu, X.: Simulation of the intraseasonal oscillation in the ECHAM-4 model: The impact of coupling with an ocean model, J. Atmos. Sci., 59(9), 1433–1453, https://doi.org/10.1175/1520-0469(2002)059<1433:SOTIOI>2.0.CO;2, 2002.

Kessler, W. S., McPhaden, M. J. and Weickmann, K. M.: Forcing of intraseasonal Kelvin waves in the equatorial Pacific, J. Geophys. Res., 100(C6), 10613–10631, https://doi.org/10.1029/95JC00382, 1995.

Khairoutdinov, M., Randall, D. and DeMott, C.: Simulations of the atmospheric general circulation using a cloud-resolving model as a superparameterization of physical processes, J. Atmos. Sci., 62(7), 2136–2154, https://doi.org/10.1175/JAS3453.1, 2005.

Khairoutdinov, M. F. and Randall, D. A.: Cloud resolving modeling of the ARM summer 1997 IOP: Model formulation, results, uncertainties, and sensitivities, J. Atmos. Sci., 60(4), 607–625, https://doi.org/10.1175/1520-0469(2003)060<0607:CRMOTA>2.0.CO;2, 2003.

455   Klingaman, N. P. and DeMott, C. A.: Mean state biases and interannual variability affect perceived sensitivities of the Madden-Julian oscillation to air-sea coupling, J. Adv. Model. Earth Syst., 12, e2019MS001799, https://doi.org/10.1029/2019MS001799, 2020.

Klingaman, N. P. and Woolnough, S. J.: The role of air-sea coupling in the simulation of the Madden-Julian oscillation in the Hadley Centre model, Q. J. Roy. Meteorol. Soc., 140(684), 2272–2286, https://doi.org/10.1002/qj.2295, 2014.

460   Klingaman, N. P., Inness, P. M., Weller, H. and Slingo, J. M.: The importance of high-frequency sea surface temperature variability to the intraseasonal oscillation of Indian monsoon rainfall, J. Climate, 21(23), 6119–6140, https://doi.org/10.1175/2008JCLI2329.1, 2008.

Klingaman, N. P., Woolnough, S. J., Weller, H. and Slingo, J. M.: The impact of finer-resolution air–sea coupling on the intraseasonal oscillation of the Indian monsoon, J. Climate, 24(10), 2451–2468, https://doi.org/10.1175/2010JCLI3868.1,
465   2011.

Large, W., McWilliams, J., and Doney, S.: Oceanic vertical mixing: A review and a model with a nonlocal boundary layer parameterization. Rev. Geophys., 32, 363–403, 1994.

Lau, W. K. M. and Waliser, D. E.: Intraseasonal variability in the atmosphere-ocean climate system, 2. ed., Springer [u.a.], Berlin., 2012.

470   Lee, J.-Y., Wang, B., Wheeler, M. C., Fu, X., Waliser, D. E. and Kang, I.-S.: Real-time multivariate indices for the boreal summer intraseasonal oscillation over the Asian summer monsoon region, Clim. Dyn., 40(1–2), 493–509, https://doi.org/10.1007/s00382-012-1544-4, 2013.

Levine, R. C. and Turner, A. G.: Dependence of Indian monsoon rainfall on moisture fluxes across the Arabian Sea and the impact of coupled model sea surface temperature biases, Clim. Dyn., 38(11–12), 2167–2190, https://doi.org/10.1007/s00382-
475   011-1096-z, 2012.

Li, J., Mao, J. and Wu, G.: A case study of the impact of boreal summer intraseasonal oscillations on Yangtze rainfall, Clim. Dyn., 44(9–10), 2683–2702, https://doi.org/10.1007/s00382-014-2425-9, 2015.

Lin, J.-L., Kiladis, G. N., Mapes, B. E., Weickmann, K. M., Sperber, K. R., Lin, W., Wheeler, M. C., Schubert, S. D., Del Genio, A., Donner, L. J., Emori, S., Gueremy, J.-F., Hourdin, F., Rasch, P. J., Roeckner, E. and Scinocca, J. F.: Tropical
480   intraseasonal variability in 14 IPCC AR4 climate models. Part I: Convective signals, J. Climate, 19(12), 2665–2690, https://doi.org/10.1175/JCLI3735.1, 2006.

Madden, R. A. and Julian, P. R.: Detection of a 40–50 Day Oscillation in the Zonal Wind in the Tropical Pacific, J. Atmos. Sci., 28(5), 702–708, https://doi.org/10.1175/1520-0469(1971)028<0702:DOADOI>2.0.CO;2, 1971.

Madden, R. A. and Julian, P. R.: Description of global-scale circulation cells in the tropics with a 40–50 day period, J.
485   Atmos. Sci., 29(6), 1109–1123, https://doi.org/10.1175/1520-0469(1972)029<1109:DOGSCC>2.0.CO;2, 1972.

Maloney, E. D.: The moist static energy budget of a composite tropical intraseasonal oscillation in a climate model, J. Climate, 22(3), 711–729, https://doi.org/10.1175/2008JCLI2542.1, 2009.

Maloney, E. D. and Hartmann, D. L.: The sensitivity of intraseasonal variability in the NCAR CCM3 to changes in convective parameterization, J. Climate, 14(9), 2015–2034, https://doi.org/10.1175/1520-0442(2001)014<2015:TSOIVI>2.0.CO;2, 2001.

Mcphaden, M. J.: Evolution of the 2002/2003 El Nino, Bulletin of the American Meteorological Society, 85, 677–695, 2004.

Moon, J.-Y., Wang, B., Ha, K.-J. and Lee, J.-Y.: Teleconnections associated with Northern Hemisphere summer monsoon intraseasonal oscillation, Clim. Dyn., 40(11–12), 2761–2774, https://doi.org/10.1007/s00382-012-1394-0, 2013.

Neena, J. M., Waliser, D. and Jiang, X.: Model performance metrics and process diagnostics for boreal summer intraseasonal variability, Clim. Dyn., 48(5–6), 1661–1683, https://doi.org/10.1007/s00382-016-3166-8, 2017.

Peatman, S. C. and Klingaman, N. P.: The Indian summer monsoon in MetUM-GOML2.0: Effects of air-sea coupling and resolution, Geosci. Model Dev., 11(11), 1–36, https://doi.org/10.5194/gmd-2018-197, 2018.

Rajendran, K. and Kitoh, A.: Modulation of tropical intraseasonal oscillations by ocean–atmosphere coupling, J. Climate, 19(3), 366–391, https://doi.org/10.1175/JCLI3638.1, 2006.

Randall, D. A., Wood, R. A., Bony, S., Colman, R., Fichefet, T., Fyfe, J., Kattsov, V., Pitman, A., Shukla, J., Srinivasan, J., Stouffer, R. J., Sumi, A., Taylor, K. E., AchutaRao, K., Allan, R., Berger, A., Blatter, H., Bonfils, C., Boone, A., Bretherton, C., Broccoli, A., Brovkin, V., Dirmeyer, P., Doutriaux, C., Drange, H., Frei, A., Ganopolski, A., Gent, P., Gleckler, P., Goosse, H., Graham, R., Gregory, J. M., Gudgel, R., Hall, A., Hallegatte, S., Hasumi, H., Henderson-Sellers, A., Hendon, H., Hodges, K., Holland, M., Holtslag, A. A. M., Hunke, E., Huybrechts, P., Ingram, W., Joos, F., Kirtman, B., Klein, S., Koster, R., Kushner, P., Lanzante, J., Latif, M., Pavlova, T., Federationi, R., Petoukhov, V., Phillips, T., Power, S., Rahmstorf, S., Raper, S. C. B., Renssen, H., Rind, D., Roberts, M., Rosati, A., Schär, C., Schmittner, A., Scinocca, J., Seidov, D., Slater, A. G., Slingo, J., Smith, D., Soden, B., Stern, W., Stone, D. A., Sudo, K., Takemura, T., Tselioudis, G., Webb, M., Wild, M., Manzini, E., Matsuno, T. and McAvaney, B.: Climate models and their evaluation, , 74, 2007.

Ren, X., Yang, X.-Q. and Sun, X.: Zonal oscillation of western Pacific subtropical high and subseasonal SST variations during Yangtze persistent heavy rainfall events, J. Climate, 26(22), 8929–8946, https://doi.org/10.1175/JCLI-D-12-00861.1, 2013.

Roxy, M., Tanimoto, Y., Preethi, B., Terray, P. and Krishnan, R.: Intraseasonal SST-precipitation relationship and its spatial variability over the tropical summer monsoon region, Clim. Dyn., 41(1), 45–61, https://doi.org/10.1007/s00382-012-1547-1, 2013.

Sabeerali, C. T., Ramu Dandi, A., Dhakate, A., Salunke, K., Mahapatra, S. and Rao, S. A.: Simulation of boreal summer intraseasonal oscillations in the latest CMIP5 coupled GCMs, J. Geophys. Res. Atmos., 118(10), 4401–4420, https://doi.org/10.1002/jgrd.50403, 2013.

Seo, K.-H., Schemm, J.-K. E., Wang, W. and Kumar, A.: The boreal summer intraseasonal oscillation simulated in the NCEP climate forecast system: The effect of sea surface temperature, Mon. Weather Rev., 135(5), 1807–1827, https://doi.org/10.1175/MWR3369.1, 2007.

Smith, D. M. and Murphy, J. M.: An objective ocean temperature and salinity analysis using covariances from a global climate model, J. Geophys. Res., 112(C2), C02022, https://doi.org/10.1029/2005JC003172, 2007.

Sperber, K. R. and Annamalai, H.: Coupled model simulations of boreal summer intraseasonal (30–50 day) variability, Part 1: Systematic errors and caution on use of metrics, Clim. Dyn., 31(2–3), 345–372, https://doi.org/10.1007/s00382-008-0367-9, 2008.

Sperber, K. R., Slingo, J. M. and Annamalai, H.: Predictability and the relationship between subseasonal and interannual variability during the Asian summer monsoon, Q. J. Roy. Meteorol. Soc., 126(568), 2545–2574, https://doi.org/10.1002/qj.49712656810, 2000.

Sperber, K. R., Gualdi, S., Legutke, S. and Gayler, V.: The Madden–Julian oscillation in ECHAM4 coupled and uncoupled general circulation models, Clim. Dyn., 25(2–3), 117–140, https://doi.org/10.1007/s00382-005-0026-3, 2005.

Sperber, K. R., Annamalai, H., Kang, I.-S., Kitoh, A., Moise, A., Turner, A., Wang, B. and Zhou, T.: The Asian summer monsoon: an intercomparison of CMIP5 vs. CMIP3 simulations of the late 20th century, Clim. Dyn., 41(9–10), 2711–2744, https://doi.org/10.1007/s00382-012-1607-6, 2013.

Stan, C., Khairoutdinov, M., DeMott, C. A., Krishnamurthy, V., Straus, D. M., Randall, D. A., Kinter, J. L. and Shukla, J.: An ocean-atmosphere climate simulation with an embedded cloud resolving model, Geophys. Res. Lett., 37(1), L01702, https://doi.org/10.1029/2009GL040822, 2010.

Waliser, D. E., Jin, K., Kang, I.-S., Stern, W. F., Schubert, S. D., Wu, M. L. C., Lau, K.-M., Lee, M.-I., Krishnamurthy, V., Kitoh, A., Meehl, G. A., Galin, V. Y., Satyan, V., Mandke, S. K., Wu, G., Liu, Y. and Park, C.-K.: AGCM simulations of intraseasonal variability associated with the Asian summer monsoon, Clim. Dyn., 21(5–6), 423–446, https://doi.org/10.1007/s00382-003-0337-1, 2003.

Wang, B., Webster, P. J. and Teng, H.: Antecedents and self-induction of active-break south Asian monsoon unraveled by satellites, Geophys. Res. Lett., 32(4), L04704, https://doi.org/10.1029/2004GL020996, 2005.

Wang, B., Webster, P., Kikuchi, K., Yasunari, T. and Qi, Y.: Boreal summer quasi-monthly oscillation in the global tropics, Clim. Dyn., 27(7–8), 661–675, https://doi.org/10.1007/s00382-006-0163-3, 2006.

Weare, B. C., Strub, P. T. and Samuel, M. D.: Annual mean surface heat fluxes in the tropical Pacific ocean, J. Phys. Oceanogr., 11(5), 705–717, https://doi.org/10.1175/1520-0485(1981)011<0705:AMSHFI>2.0.CO;2, 1981.

Weaver, S. J., Wang, W., Chen, M. and Kumar, A.: Representation of MJO variability in the NCEP climate forecast system, J. Climate, 24(17), 4676–4694, https://doi.org/10.1175/2011JCLI4188.1, 2011.

Wheeler, M. and Kiladis, G. N.: Convectively coupled equatorial waves: Analysis of clouds and temperature in the wavenumber–frequency domain, J. Atmos. Sci., 56(3), 374–399, https://doi.org/10.1175/1520-0469(1999)056<0374:CCEWAO>2.0.CO;2, 1999.

Woolnough, S. J., Vitart, F. and Balmaseda, M. A.: The role of the ocean in the Madden–Julian oscillation: Implications for MJO prediction, Q. J. Roy. Meteorol. Soc., 133(622), 117–128, https://doi.org/10.1002/qj.4, 2007.

Wu, X., Deng, L., Song, X., Vettoretti, G., Peltier, W. R. and Zhang, G. J.: Impact of a modified convective scheme on the Madden-Julian Oscillation and El Niño-Southern Oscillation in a coupled climate model, Geophys. Res. Lett., 34(16), L16823, https://doi.org/10.1029/2007GL030637, 2007.

Yasunari, T.: Cloudiness fluctuations associated with the northern summer monsoon, J. Meteorol. Soc. Japan, 57(3), 16, 1979.

Zhang, C.: Madden-Julian oscillation, Rev. Geophys., 43, RG2003, https://doi.org/10.1029/2004RG000158, 2005.

Zhang, C. and Gottschalck, J.: SST anomalies of ENSO and the Madden–Julian oscillation in the equatorial Pacific, J. Climate, 15(17), 2429–2445, https://doi.org/10.1175/1520-0442(2002)015<2429:SAOEAT>2.0.CO;2, 2002.

Zhang, C., Dong, M., Gualdi, S., Hendon, H. H., Maloney, E. D., Marshall, A., Sperber, K. R. and Wang, W.: Simulations of the Madden–Julian oscillation in four pairs of coupled and uncoupled global models, Clim. Dyn., 27(6), 573–592, https://doi.org/10.1007/s00382-006-0148-2, 2006.

Table 1: List of simulations analyzed in this study, including the name used in the text, model, type, and ocean climatology condition to which the model is constrained (coupled model) or prescribed (atmospheric-only model).

Name	Model	Type	Ocean surface
SPK-OBS	SPCAM3-KPP	CGCM	Climatology from observation
SPK-SPC	SPCAM3-KPP	CGCM	Climatology from SPCCSM3
SPA-KOBS	SPCAM3	AGCM	31-day smoothed SST from SPK-OBS
SPA-KSPC	SPCAM3	AGCM	31-day smoothed SST from SPK-SPC
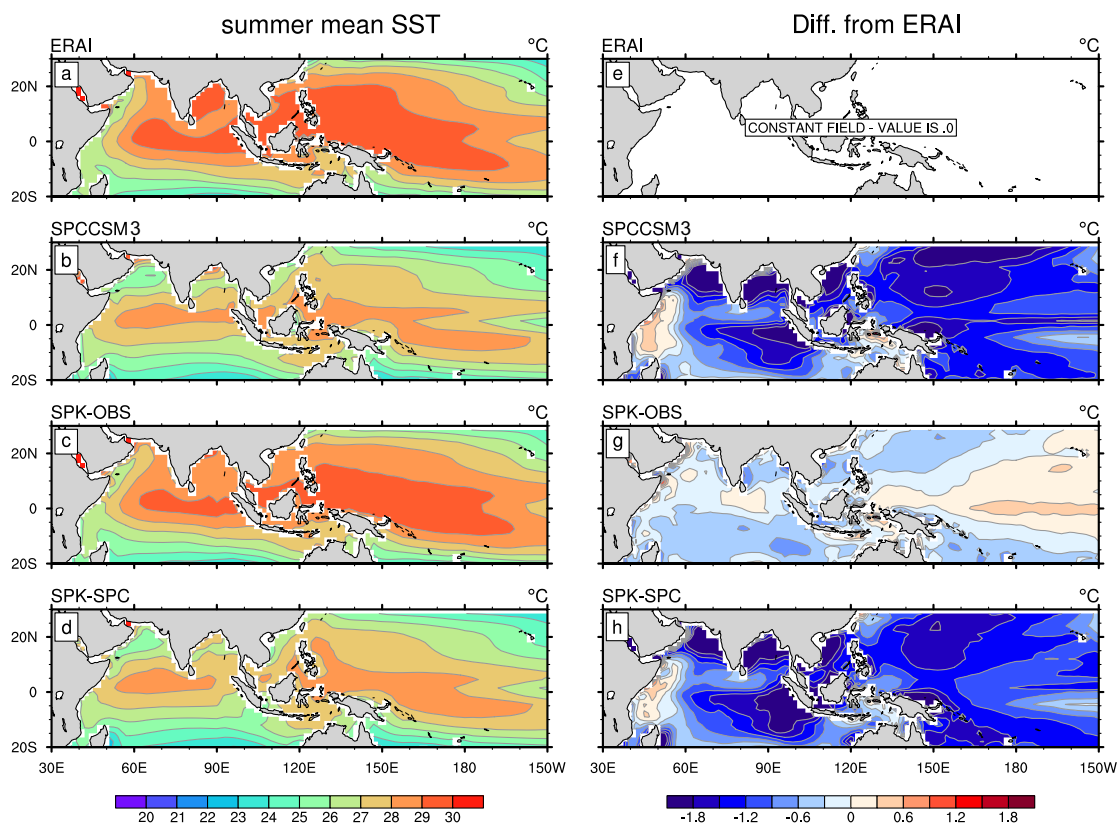
Figure 1: May–October mean SST for (a) ERAI, (b) SPCCSM3, (c) SPK-OBS, and (d) SPK-SPC. (e)–(h) are calculated as the difference between (a)–(d) and (a).
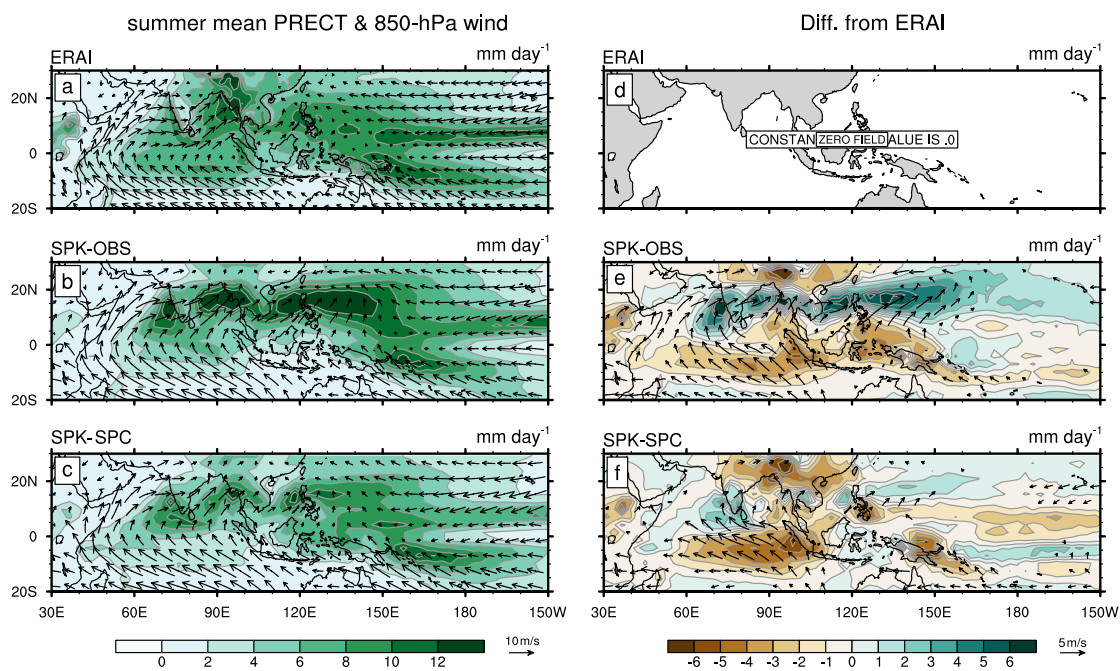
Figure 2: May–October mean precipitation (shading) and 850-hPa wind (vectors; with amplitude > 1 m s^{-1}) for (a) ERAI, (b) SPK-OBS and (c) SPK-SPC. (d)–(f) are calculated as the difference between (a)–(c) and (a).
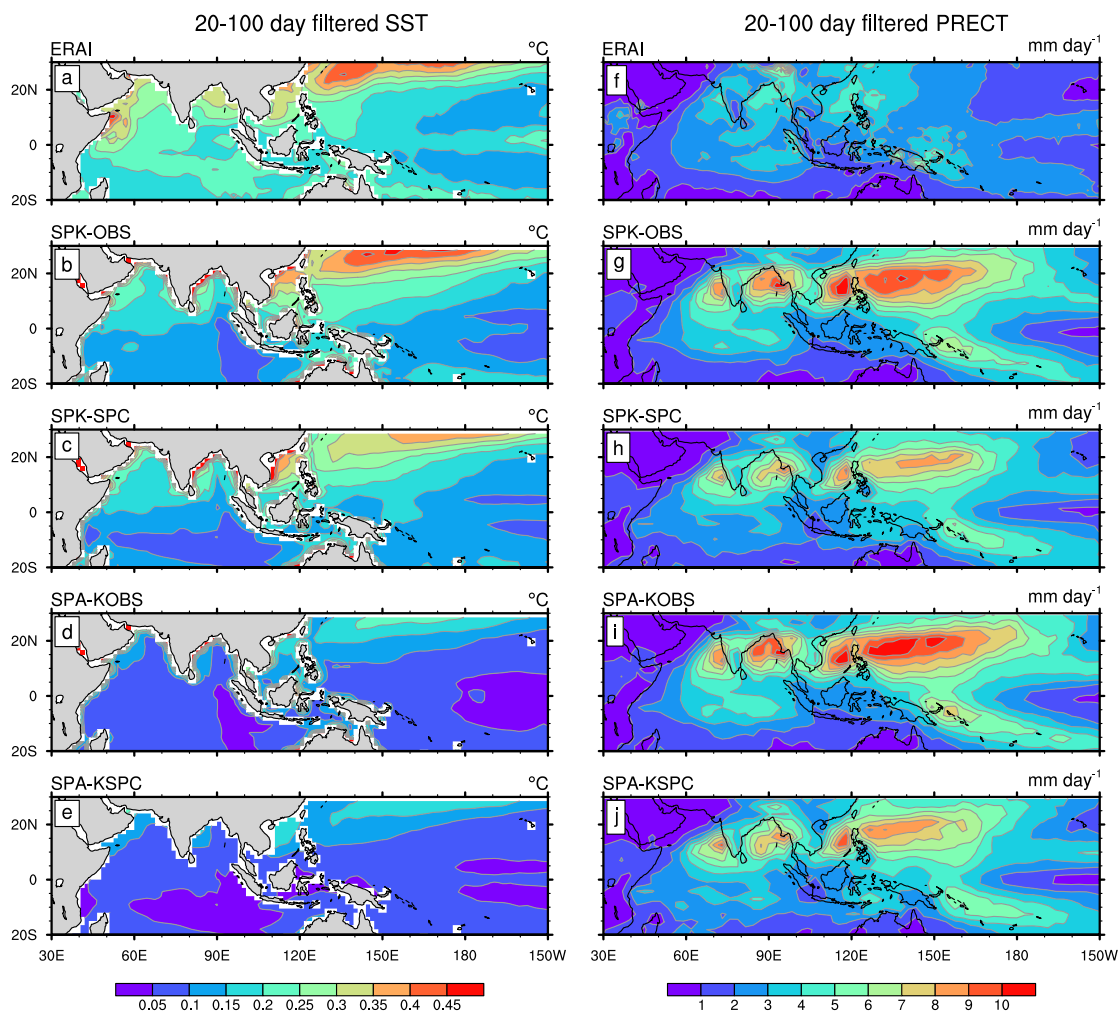
Figure 3: May–October standard deviations of 20–100-day-filtered (left column) SST and (right column) precipitation for (a, f) ERAI, (b, g) SPK-OBS, (c, h) SPK-SPC, (d, i) SPA-KOBS, and (e, j) SPA-KSPC.
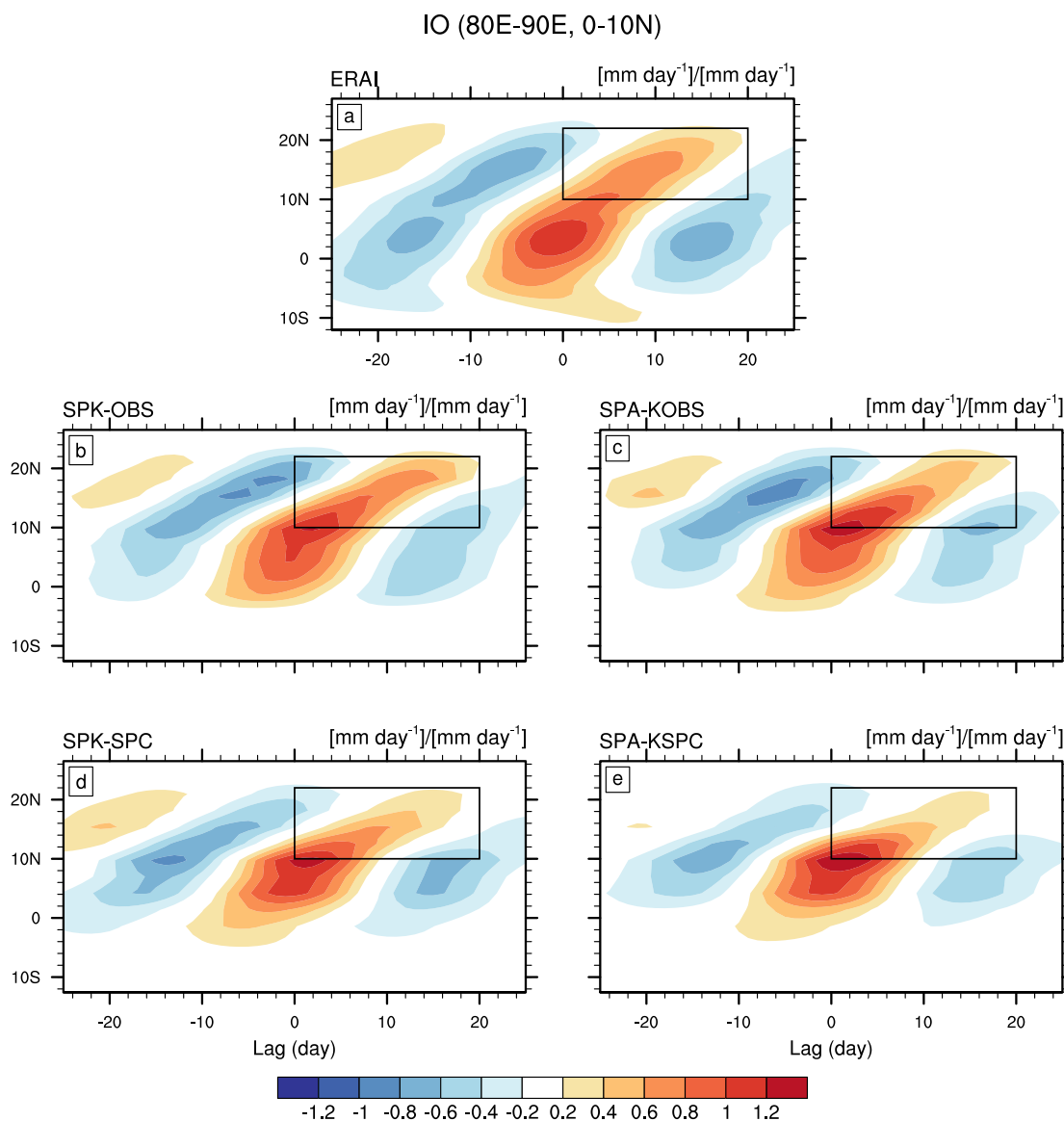
IO (80E-90E, 0-10N)

Figure 4: Lagged regression coefficients of 80°E–90°E averaged intraseasonal precipitation onto (80°E–90°E, 0°–10°N) averaged intraseasonal precipitation for (a) ERAI, (b) SPK-OBS, (c) SPA-KOBS, (d) SPK-SPC, and (e) SPA-KSPC. Black box in each panel denotes (10°N–22°N, Lags 0–20).
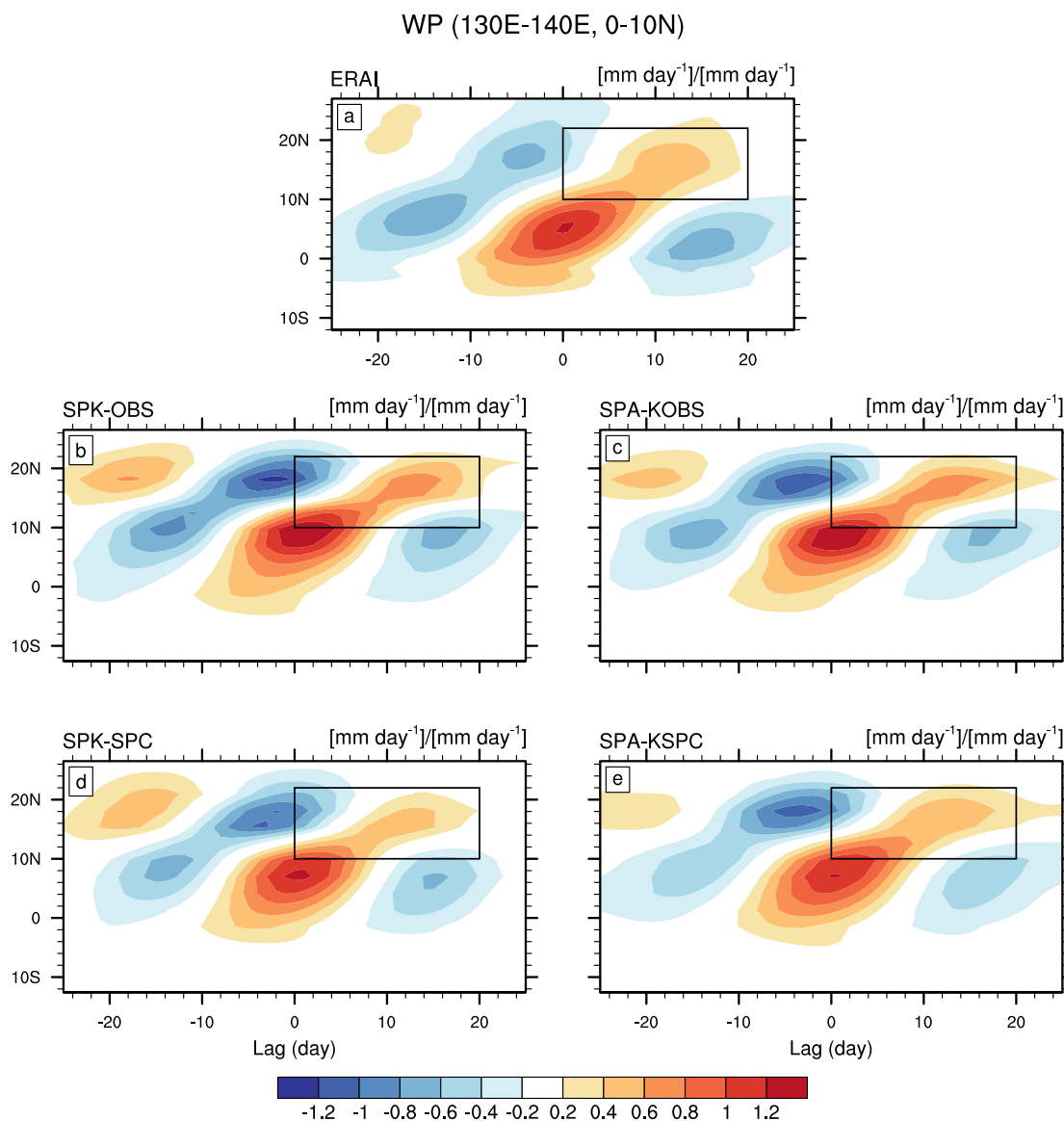
Figure 5: As in Fig. 4, except for 130°E–140°E averaged intraseasonal precipitation regressed onto (130°E–140°E, 0°–10°N) averaged intraseasonal precipitation.
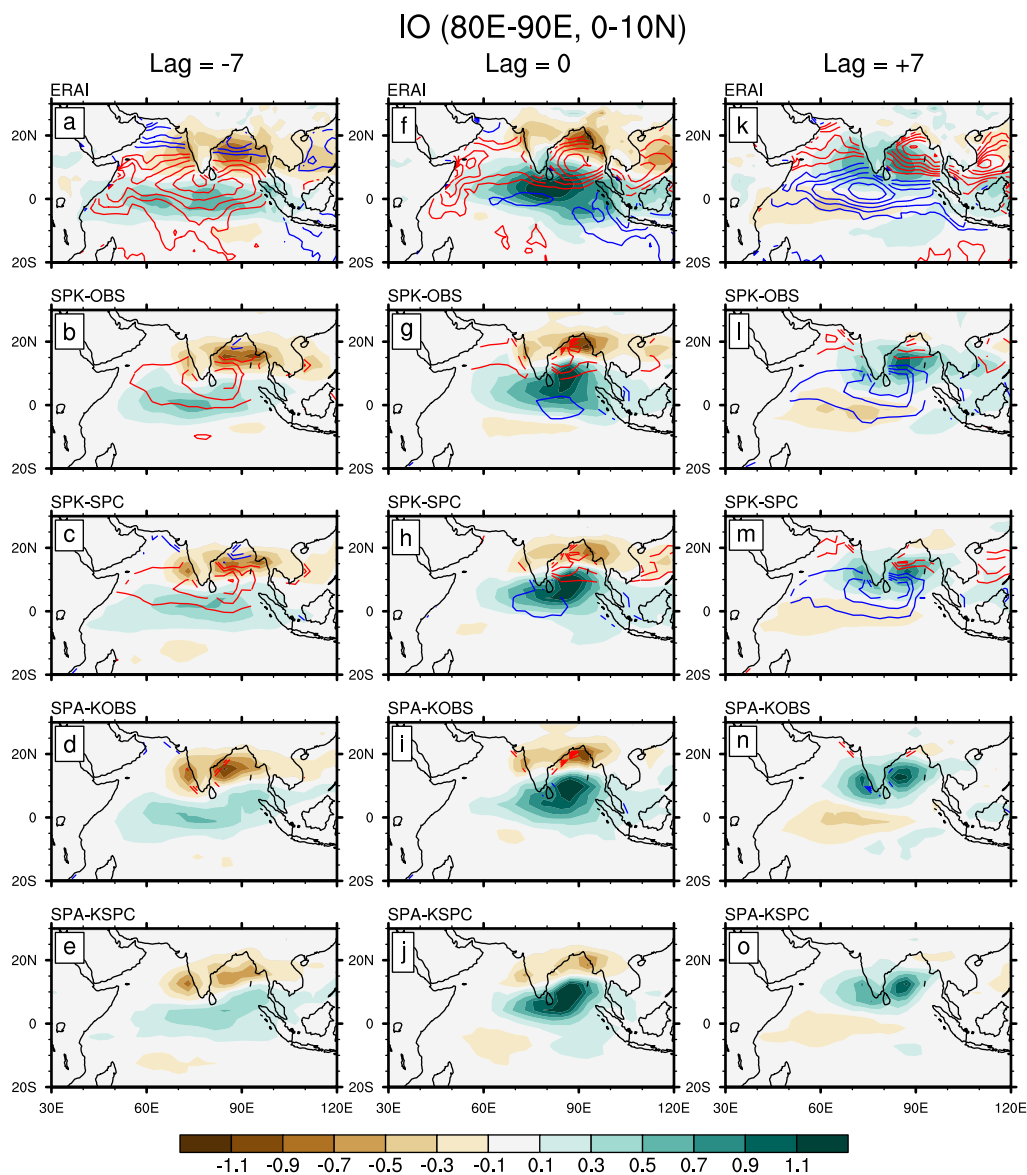
Figure 6: Regression coefficients of intraseasonal precipitation (shading; [mm day^{-1}]/[mm day^{-1}]) and SST (contours; [°C]/[mm day^{-1}]) onto (80°E–90°E, 0°–10°N) averaged intraseasonal precipitation over the Indian Ocean at lags of (left column) -7, (middle column) 0 and
595 (right column) +7 days, for (a, f, k) ERAI, (b, g, l) SPK-OBS, (c, h, m) SPK-SPC, (d, i, n) SPA-KOBS, and (e, j, o) SPA-KSPC. The contour interval is 0.01 [°C]/[mm day^{-1}], positive (negative) values are represented by red (blue) lines.
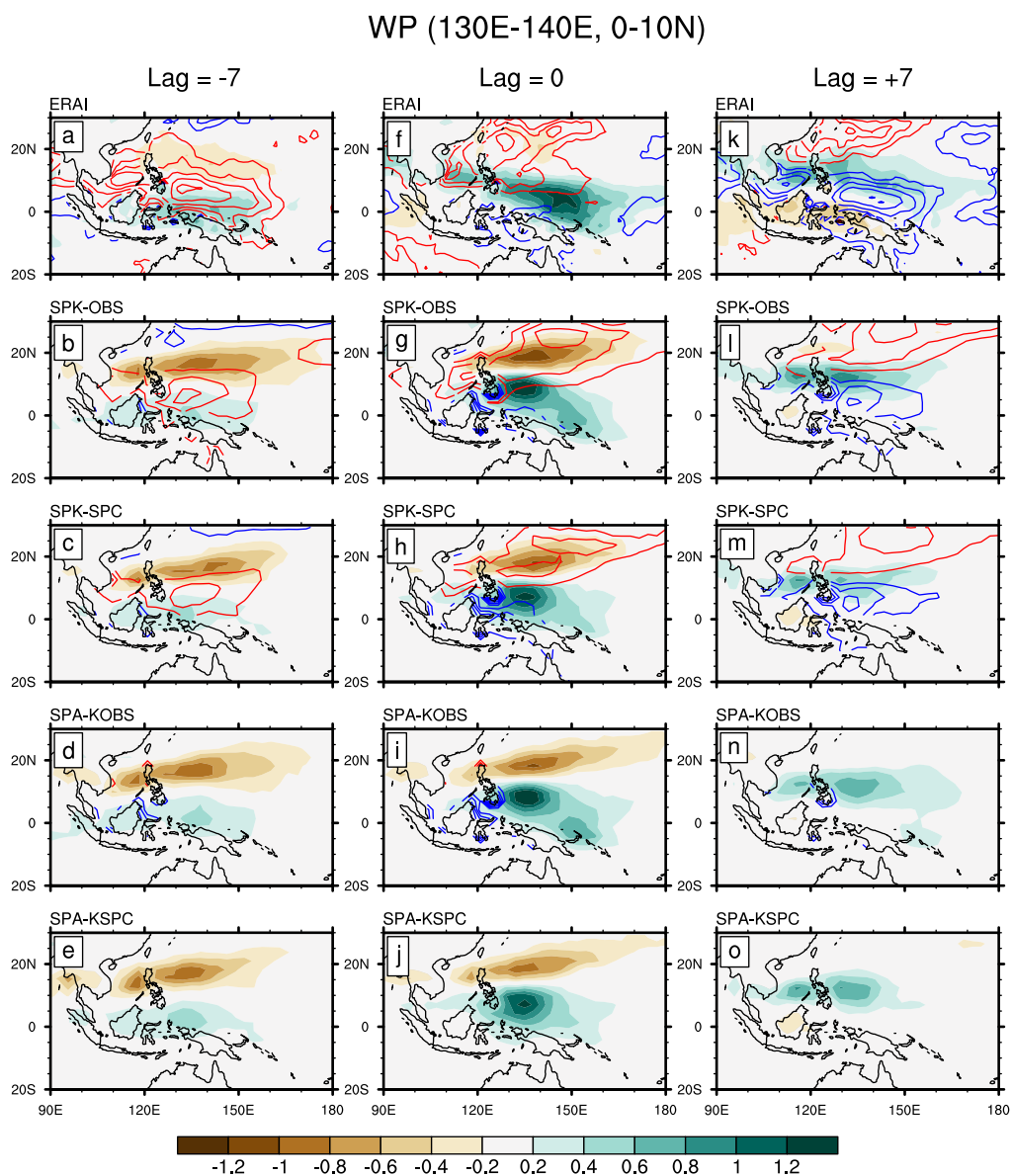
Figure 7: As in Fig. 6, except for variables regressed onto (130°E–140°E, 0°–10°N) averaged intraseasonal precipitation over the western Pacific.

SST effect
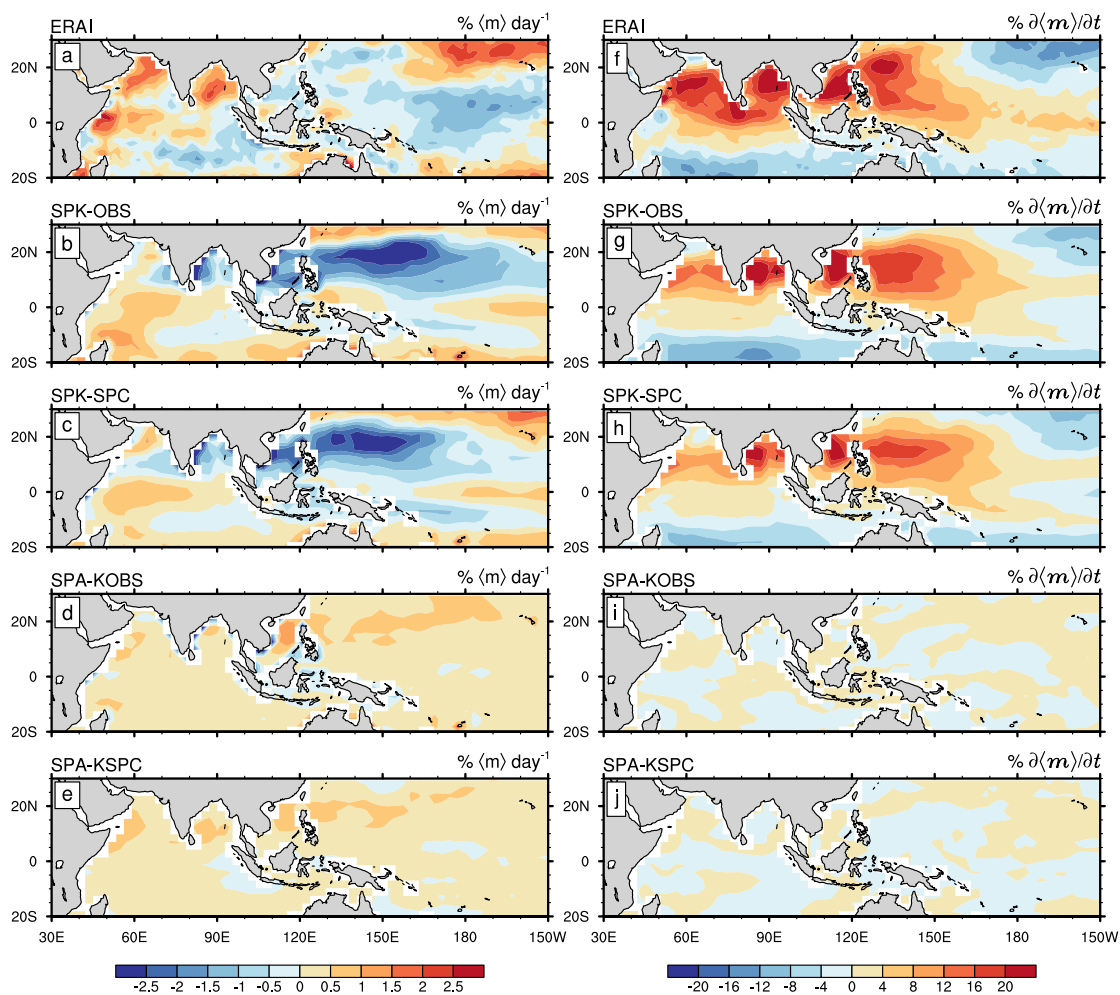
Figure 8: The SST effect on (left column) $\langle m \rangle$ and (right column) $\partial \langle m \rangle / \partial t$ through the modification of surface turbulent fluxes for (a, f) ERAI, (b, g) SPK-OBS, (c, h) SPK-SPC, (d, i) SPA-KOBS, and (e, j) SPA-KSPC.

605
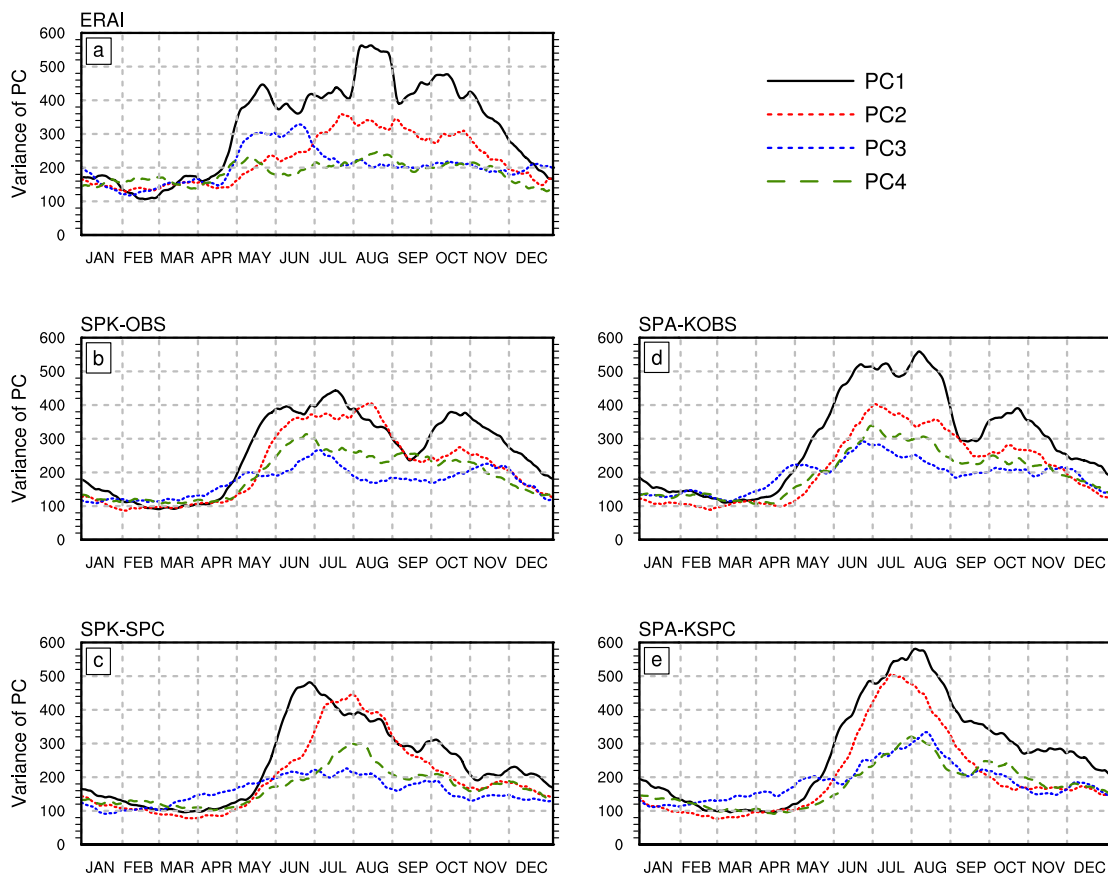
Figure 9: The seasonal cycle of variance of the leading four PCs for (a) ERAI, (b) SPK-OBS, (c) SPK-SPC, (d) SPA-KOBS, and (e) SPA-KSPC. A 30-day running mean is applied to the seasonal cycle of each dataset.
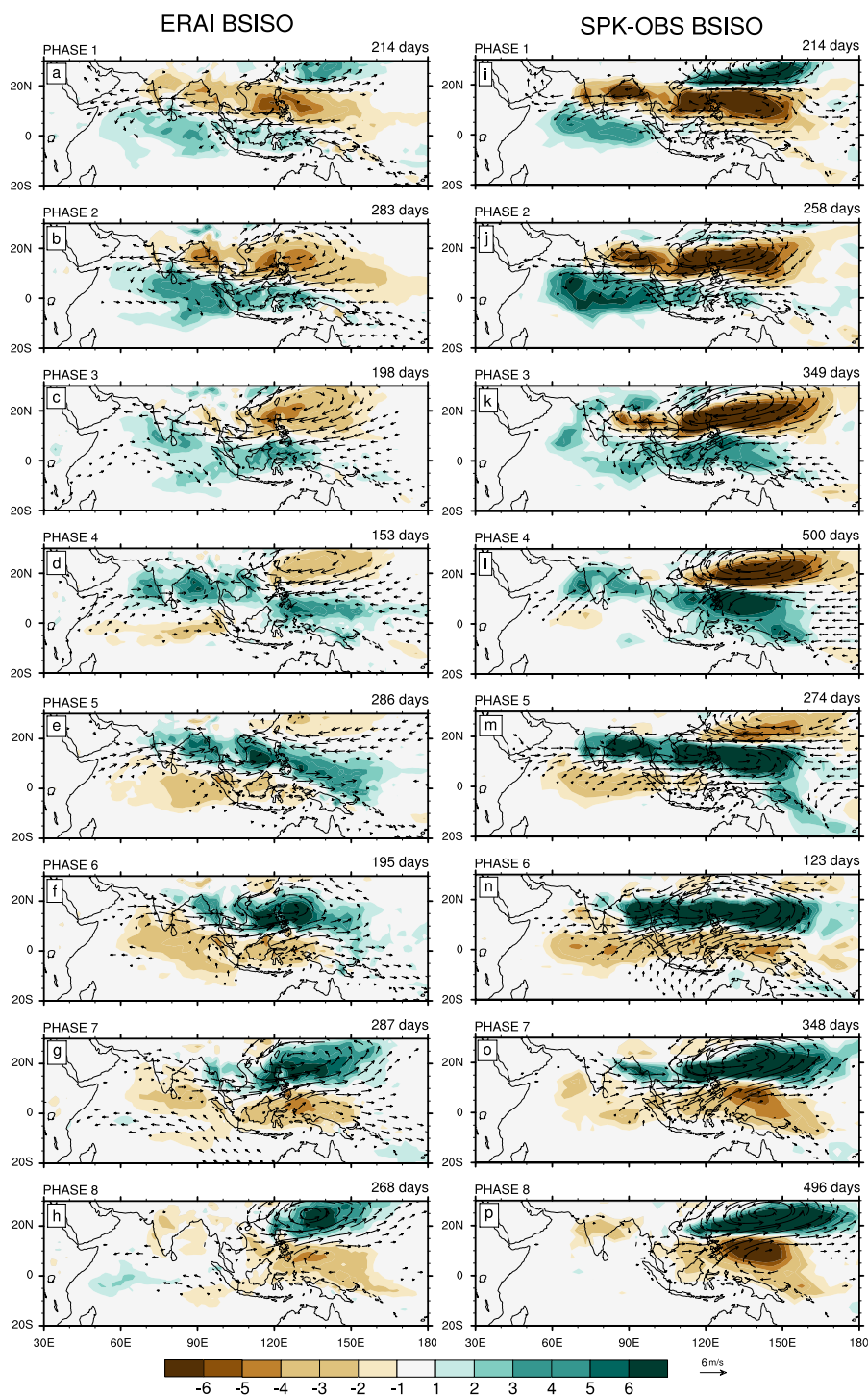
Figure 10: Composites of anomalous precipitation (shading; mm day^{-1}) and 850-hPa wind (vectors; with amplitude > 1 m s^{-1}) in the BSISO life cycle from phase 1 to phase 8 for (a–h) ERAI and (i–p) SPK-OBS. The number of days for phase composite is shown in the right corner above each panel. Only strong BSISO events (amplitude ≥ 1.5) are selected.
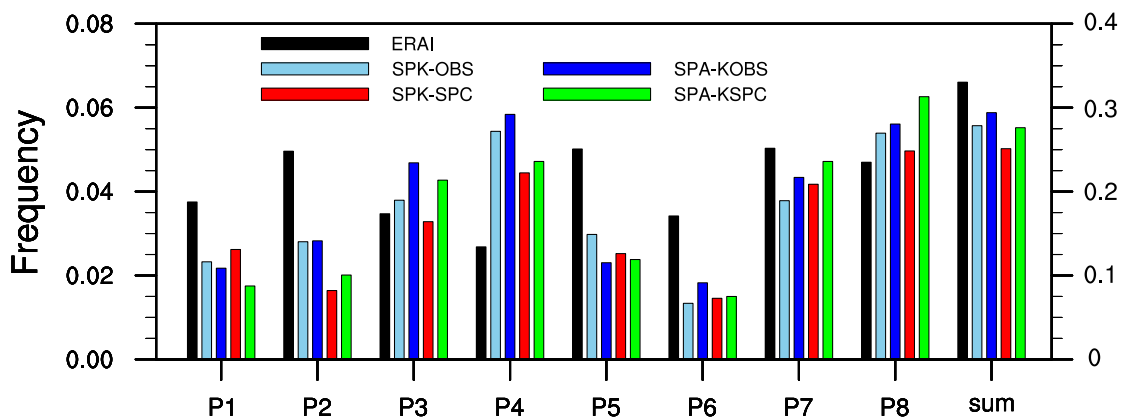
615 **Figure 11:** The frequency of strong BSISO activity (amplitude ≥ 1.5) in each phase (P1–P8; in the left y-axis) and their sum (in the right y-axis) for ERAI (black), SPK-OBS (light blue), SPK-SPC (red), SPA-KOBS (dark blue) and SPA-KSPC (green).
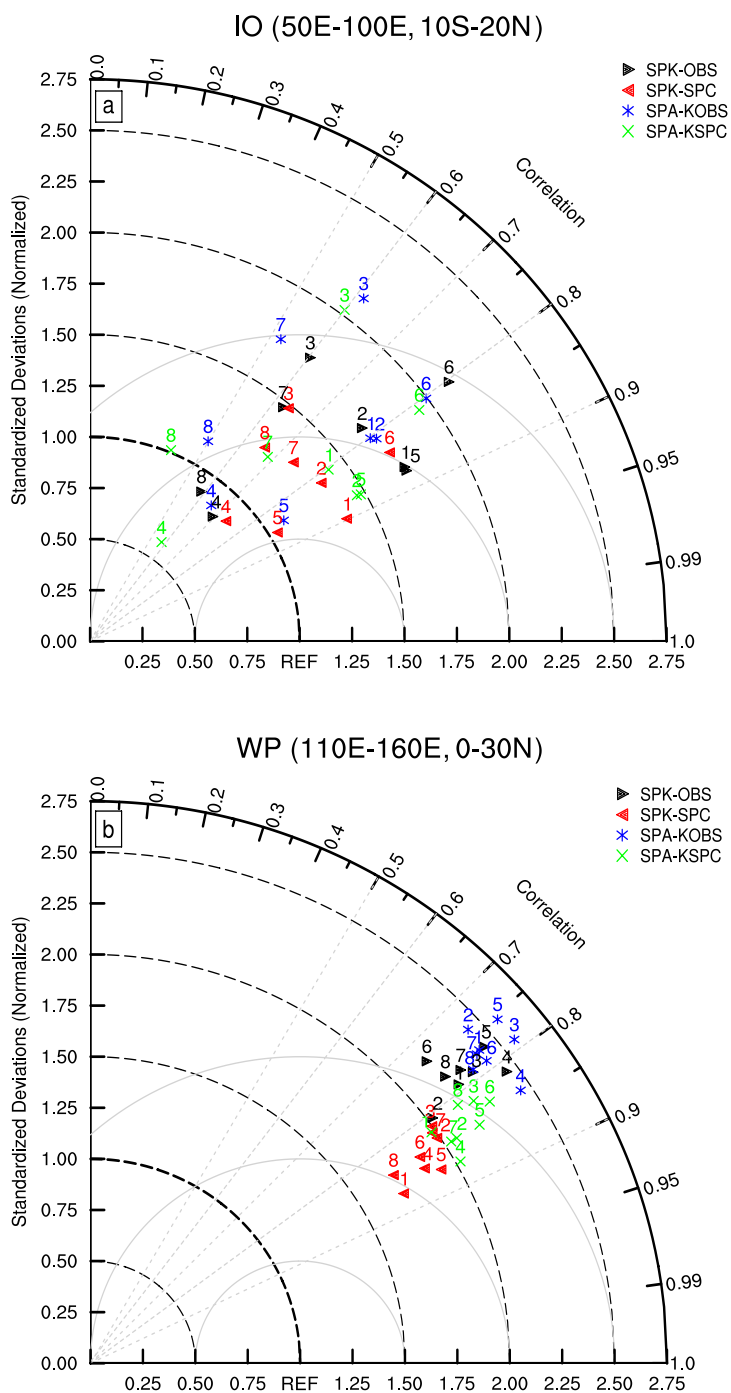
Figure 12: Taylor diagrams for anomalous precipitation in each BSISO phase averaged over the (a) Indian Ocean (IO; 50°E–100°E, 10°S–20°N) and (b) western Pacific (WP; 110°E–160°E, 0°–30°N). The number above each symbol refers to the BSISO phase.